Hindawi
International Journal of Photoenergy
Volume 2020, Article ID 7095872, 9 pages
https://doi.org/10.1155/2020/7095872

Research Article

Study on Tensile Creep Behavior of 12Cr1MoV Alloy Steel under High-Temperature Alkali Metal Salt Environment for Solar Thermal Power Generation

Jianjun He, Kaijun Yang, Gang Wang, Wei Li, Jiangyong Bao, and Jian Chen

School of Energy and Power Engineering, Changsha University of Science and Technology, Changsha, Hunan 410114, China

Correspondence should be addressed to Jianjun He; hejianjun@csust.edu.cn

Received 30 September 2019; Revised 5 January 2020; Accepted 15 February 2020; Published 13 March 2020

Academic Editor: Joaquim Carneiro

The heat exchange tubes of solar thermal power generation work in molten salt environment with periodic temperature change. In order to reveal the tensile creep behavior of 12Cr1MoV pipeline steel under high-temperature alkali metal salt environment, the tensile creep behavior of 12Cr1MoV alloy under different applied load and reaction temperature in high-temperature alkali metal chloride salt environment was studied. The results show that the deformation of 12Cr1MoV alloy in 600°C, NaCl-35%KCl mixed salt environment is mainly controlled by diffusion creep; with the increase of stress, the creep life of 12Cr1MoV alloy decreases. The creep fracture mechanism of 12Cr1MoV alloy in 600°C, NaCl-35%KCl mixed salt environment is intergranular ductile fracture; the increase of temperature will enhance the activation and oxidation of the chlorine atoms, thereby accelerating the corrosion of the base metal and increasing the spheroidization speed of the pearlite matrix, and the creep deformation rate of the alloy increases with increasing temperature.

1. Introduction

12Cr1MoV as an alloy material with high strength and good heat resistance [1–3] has been widely used in solar thermal power generation heat exchange tubes. Compared with coal and other fossil fuels, solar thermal power generation has the advantages of high power generation efficiency and strong controllability [4]. However, the heat storage material in solar thermal power generation contains a certain amount of potassium and chlorine, which causes certain corrosion to the heat exchange tubes in the solar thermal power station in the molten state, thereby affecting the service life of the entire system [5–7]. At the same time, heat pipes will be deformed by the high-temperature stress and steam pressure [8]. In actual service conditions, heat pipes will experience both hot corrosion and creep attack, and such combined effects were studied recently.

The creep properties of salt-coated alloy are available in literatures. Most studies mainly focus on the influence of a single saline environment on creep rupture life, deformation mechanisms of alloy, and creep properties [9]. Various factors that reduce the creep life of alloys by thermal corrosion, such as the generation and propagation of surface cracks, have been confirmed by previous studies. The creep fracture behavior of Nimonic-90 alloy at high-temperature and hot corrosion environment was studied by Gosh [10]. The results show that the minimum creep rate will increase and the creep life will decrease under the corrosive condition. A large number of cracks and defect structures are produced in the surface of the material, then sprout and expand into the interior, due to the oxidation, sulfidation, and chlorination reactions occurring simultaneously. There is a dispute over whether different alkali metal salts affect the creep behavior of materials. Suryanarayanan et al. [11] indicated that the creep life of the material is reduced in different corrosion conditions, especially in the NaCl-Na_2SO_4 mixed salt. Bagui et al. [12] show that the creep progress will be accelerated in mixed salt and high-temperature environment, but no significant effect on creep progress with different proportion of NaCl-Na_2SO_4 mixed salt. In the current study, on He and Xiong's point of view [13], it is interesting to note that creep deformation of microstructures in NaCl-40%Na_2SO_4 was the

Table 1: Chemical compositions of 12Cr1MoV steel (wt.%).

C	Si	Cr	Mn	Mo	V
0.08~0.15	0.17~0.37	0.90~1.20	0.40~0.70	0.25~0.35	0.15~0.30

Table 2: Tensile creep test scheme of 12Cr1MoV alloy in alkali metal salt environment with different stresses.

Number	Temperature (°C)	Stress (MPa)	Salt mixture
1#	600	200	NaCl-35%KCl
2#	600	215	NaCl-35%KCl
3#	600	230	NaCl-35%KCl

weakest, indicating that sulfates can suppress corrosion of molten chlorides. However, the specimens in chloride mixture show relatively high compression creep strain and steady-state creep rate compared with the bare specimens, and this effect accelerates with the increase of temperature.

A considerable research has been done to determine the creep properties and creep crack behavior through the tensile creep test under high-temperature corrosion conditions. However, the interaction between creep and high-temperature corrosion has not been well verified. In this paper, the effect of hot corrosion damages on compression creep properties of 12Cr1MoV alloy was investigated at different range of temperature and tensile stresses in NaCl-35%KCl mixture. This study is aimed at investigating the influence of interaction between hot corrosion and creep properties.

2. Materials and Methods

The heat-treated 12Cr1MoV heat pipe steel is chosen as the raw material in this experiment. The chemical components are shown in Table 1.

Alkali metal chloride is the main cause of corrosion on the surface of heat exchange tubes during solar thermal power generation [14]. NaCl-35%KCl is selected as hot corrosion environment in our experiments. The study of the relationship between tensile creep property and stress of solar thermal power exchange tube under high-temperature alkali metal conditions has important engineering significance. Therefore, the tensile creep tests under different stress conditions at high-temperature alkali metal environment were designed, as shown in Table 2.

Similarly, temperature has an important effect on the corrosion rate of the solar thermal power exchange tube. Therefore, the experimental scheme of tensile creep of the sample in the high-temperature alkali metal salt at different temperatures is designed, as shown in Table 3.

The experimental equipment is an electronic creep relaxation tester RDL100 manufactured by Changchun Mechanical Science Research Institute Co., Ltd., equipped with an EDC222 controller manufactured by German DOLI company and an AI-808 temperature controller. The surface of the sample was coated with a layer of salt film. All specimens are insulated at experimental temperature for 30 min before experiment to ensure uniform heating.

Table 3: Tensile creep test scheme of 12Cr1MoV alloy in alkali metal salt environment at different temperatures.

Number	Temperature (°C)	Stress (MPa)	Salt mixture	Time (h)
4#	560	200	NaCl-35%KCl	41.8
5#	580	200	NaCl-35%KCl	41.8
6#	600	200	NaCl-35%KCl	41.8
7#	600	200	Air	41.8

3. Results and Discussion

3.1. Creep Curves. Figure 1 shows the relationship between the creep strain and time (creep curves) of 12Cr1MoV in different conditions. It can be seen from Figure 1(a) that there are three typical stages in the creep process. With the increase of pressure, the time of the steady-state creep stage is obviously reduced, and the creep stage enters the accelerated creep stage from the deceleration creep stage, which leads to the fracture failure of the specimen. The creep strains of the three specimens were 0.149, 0.195, and 0.229, respectively, and the steady-state creep rates were 0.913×10^{-3}/h, 1.12×10^{-3}/h, and 1.91×10^{-3}/h, respectively. The results show that the tensile stress has a significant influence on the creep deformation, and the strain value decreases with the increase of the applied load at the hot corrosion specimen.

As shown in Figure 1(b), tensile creep tests of three groups of specimens at different temperatures were carried out in 41.8 h. At 600°C, the sample is broken and the tensile creep strain is about 0.149. However, other two samples at 560°C and 580°C are still in the steady creep stage, there is no obvious instability phenomenon that occurred, and the tensile creep strains of them are only 0.00402 and 0.0136, respectively. By calculating, at the temperature of 560°C, 580°C, and 600°C, the steady creep rates of three specimens are 0.5467×10^{-4}/h, 2.385×10^{-4}/h, and 9.125×10^{-4}/h, respectively.

Figure 1(c) is the tensile creep curve of the sample in a mixed salt and salt-free environment at a high temperature of 600°C. Under the same experimental time, there are three complete creep stages in the specimens at the mixed salt environment, while the specimens in salt-free environment are still in the steady-state creep stage. It can be seen from the creep curve that during the first 15 h tensile test, the effect of the presence or absence of salt on the creep is not significant. With the progress of the experiment, the salt-coated samples quickly transitioned from the steady-state creep phase to the accelerated creep phase, until they failed and fractured, the salt-free sample maintains a stable creep strain rate and is still in the steady-state creep stage during the experiment.

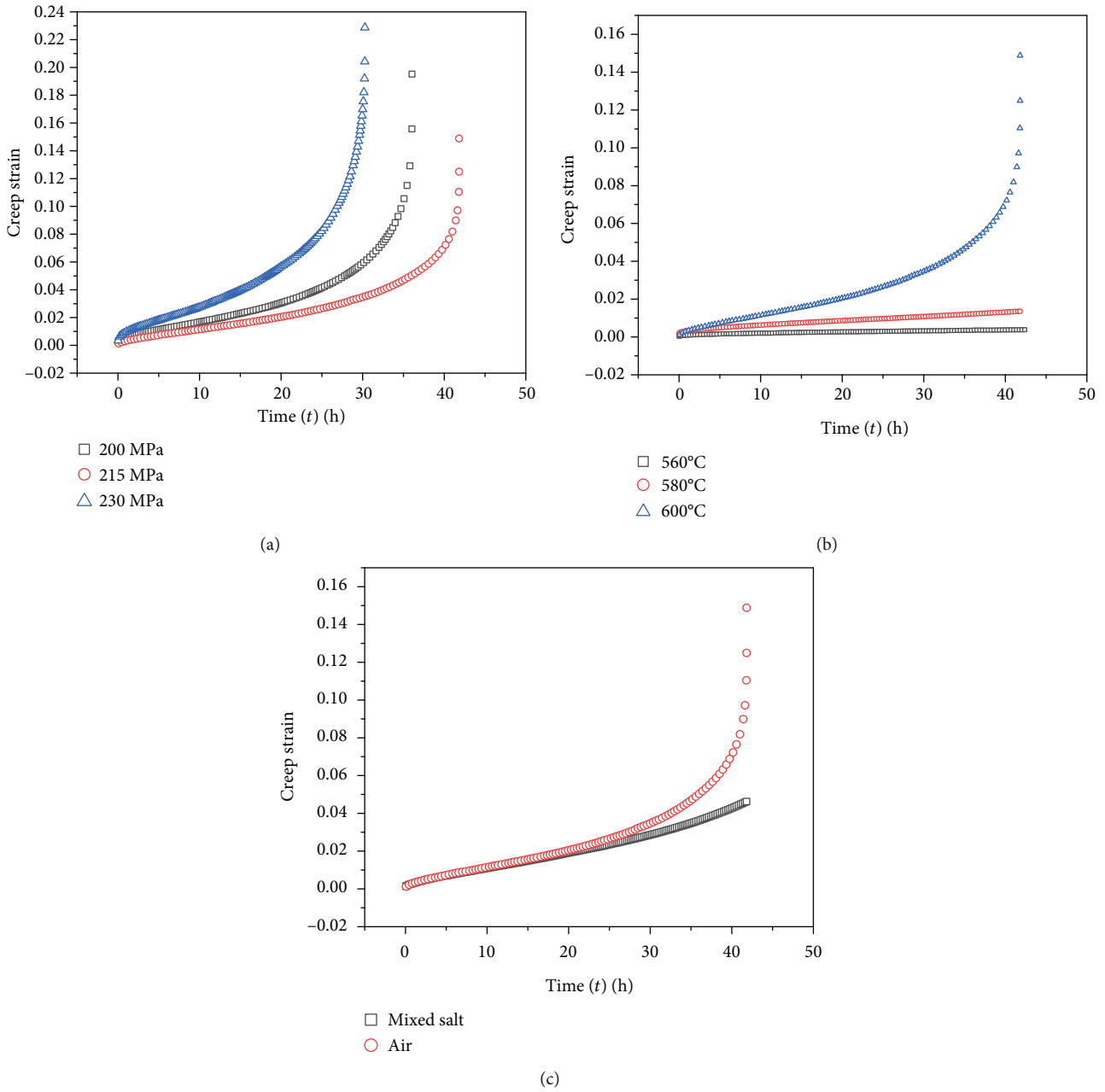

Figure 1: Creep curves in different conditions: (a) influence of applied tensile stress and constant temperature of 600°C, (b) influence of temperature and constant tensile stress of 200 MPa, and (c) influence of corrosion environment at an applied tensile stress of 200 MPa and temperature of 600°C.

3.2. Creep Stress Exponent. The relationship between creep rate $\dot{\varepsilon}$, stress σ, and temperature T in the steady-state creep stage can be expressed by power law creep constitutive equation:

$$\dot{\varepsilon} = A\sigma^n \exp\left(-\frac{Q_C}{RT}\right), \tag{1}$$

where $\dot{\varepsilon}$ is the steady-state creep rate, A is a constant related to material characteristics, σ is the creep stress applied, Q_C is the apparent creep activation energy (kJ/mol), and R is the molar gas constant with a value of 8.314 J/(mol·K), T is the thermodynamic temperature. When the temperature or stress is constant, the stress exponent and apparent creep activation energy can be expressed as

$$n = \left(\frac{\partial \ln \dot{\varepsilon}}{\partial \ln \sigma}\right)_T,$$
$$Q_C = -R\left[\frac{\partial \ln \dot{\varepsilon}}{\partial (1/T)}\right]_\sigma. \tag{2}$$

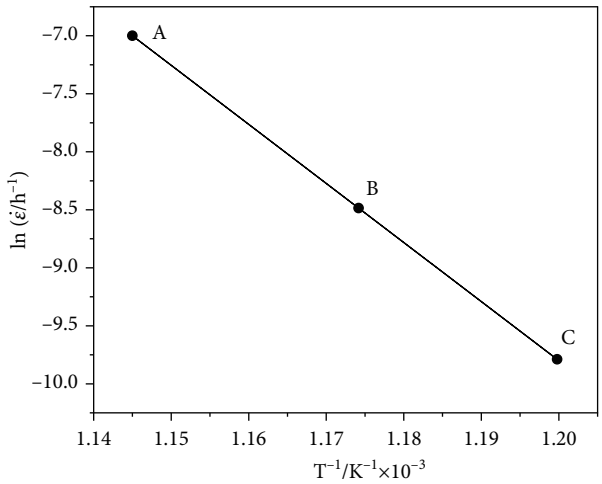

Figure 2: Fitting relationship of $\ln \dot{\varepsilon}$ and $1/T$ for samples 4#, 5#, and 6# at different temperatures under the same stress (points A, B, and C correspond to the creep rates calculated for samples 4#, 5#, and 6#, respectively).

Based on the above discussion, it can be found that the creep stress exponent of 200-230 MPa is 0.12. A large number of studies have shown that the stress exponent is directly related to the creep deformation mechanism. The material deformation is controlled by the diffusion creep mechanism at $n = 1$, the material deformation is a dislocation slip mechanism at $n = 3$, the material deformation is dislocation climb mechanism in high-temperature environment at $n = 5$, and the material deformation is the dislocation climb mechanism at low temperature at $n = 7$ [9]. The stress exponent of this experiment is close to 1 in the above creep deformation mechanism. Therefore, the tensile creep deformation of 12Cr1MoV alloy is controlled by diffusion creep under the condition of 600°C, NaCl-35%KCl. The $\ln \dot{\varepsilon}$ and $1/T$ relationship curve is shown in Figure 2; the apparent creep activation energy is 425.6 kJ/mol by calculation.

3.3. Fracture Appearance. Figure 3 shows creep fracture morphology at high temperature in alkali metal salt environment under different stress conditions. Necking phenomenon can be observed in these three figures. The central region of the fracture perpendicular to the tensile stress is the fiber region, which is the starting point of the fracture; the nucleation occurs, grows, and aggregates in this region; thus, a deep hole can be observed, and the cracks radiate from the center to the periphery with flower shape. When the cracks extend to the surface, all specimens occur obvious shear lips which form certain angle with the tensile stress direction. The morphology shows a typical cup cone fracture, which can be judged as ductile fracture. It can be seen that with the increase of tensile stress, the proportion of the shear lip and fiber zone decreases while the proportion of radiation zone increases. Combined with the creep curve of Figure 1(a), it is found that greater stress results in larger radiation zone and shorter steady-state creep time.

Figure 4 is the fracture morphology of the samples in 200 MPa and 230 MPa, respectively. It can be seen that the tensile creep rupture fracture mainly distributes dimples which have different shapes and sizes under different stress conditions at high temperature. The size and depth of the dimples are related to the number of voids and plasticity of the void core when the material breaks. If the dimple has a lot of nucleation sites or the material is poorly plasticized, the dimples formed at the time of the fracture are smaller and shallower. Or the dimples are bigger and deeper [10].

Comparing Figures 4(a) and 4(b), the colony boundary is indicated by a red dotted line, dimple size of specimen 1# (200 MPa) is larger than specimen 3# (230 MPa), the area of the colony boundary is smaller, and the cracks primarily propagate along the colony boundary. The stress has a direct influence on the plastic deformation ability of the material. The lower the stress, the better the plasticity and the better the toughness.

3.4. Microstructural Change

3.4.1. Microstructure of Section Areas. Figure 5 reveals microstructure characteristics of cross sections where corrosion depth and internal attack can be reflected with mixed salt or salt-free environments at different temperatures. Temperature has significant effect on the microstructure of the section. The load stress is set as 200 MPa. The samples are corroded by alkali metal salt at the high temperature, and the corrosion layer presents a hierarchical structure. The crack direction of corrosion layer is consistent with the direction of loading stress. The outer layer and the second outer corrosion are porous oxide which are easy to fall off. The inner layer, as the boundary layer between oxide and substrate organization, is not completely corroded. The thickness of the corrosion layer at 600°C is about 600 μm, while it is only 30 μm at 560°C. It is shown that with the increase of temperature, more metal matrix is corroded by alkali metal salt, and the interface between the matrix and the corrosion layer will gradually advance to the center of the matrix. In salt-free environment, the oxide layer formed by thermal oxidation is relatively dense and fuzzy and suggests a protective role. Energy-dispersive X-ray spectroscopy (EDS) analytical technique was employed to perform the elemental analysis of the inner and outer corrosion layers; the equipment used was called field emission scanning electron microscope, and the results are presented in Table 4.

According to Table 4, the corrosion outer layer mainly contains Fe, O, and a small amount of Cr, Cl, and Si. Meanwhile, 2.78% of Cr and 1.05% of Cl in the corrosion inner layer were detected. The results show that the Cr_2O_3 and SiO_2 protective oxide layers formed between the corrosion inner layer and the base layer are destroyed by high-temperature chloride corrosion, resulting in cracking, crushing, and peeling. In contrast to the study on chloride corrosion of alkali metal [15], the destruction mechanism of 12Cr1MoV in high-temperature chlorine salt mixture is the activation oxidation behavior of Cl. Activated oxidation is the process of gradual destruction of the chloride from the surface to the base layer at high temperature. As long as the chloride salt is sufficient and has a certain oxygen partial pressure, the oxidation reaction in the material is equivalent

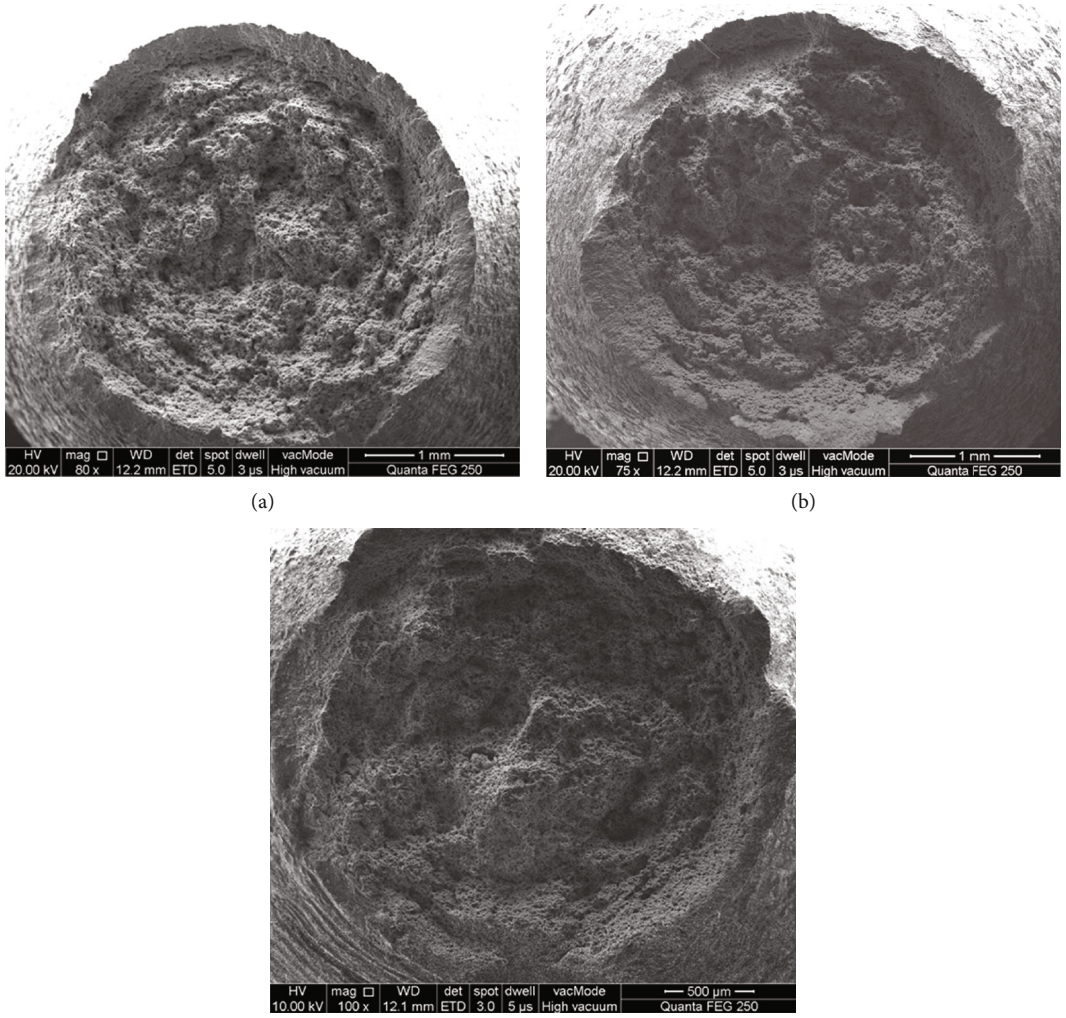

(a) (b)

(c)

Figure 3: Macroscopic morphology of fracture with different stresses: (a) 1# (200 MPa), (b) 2# (215 MPa), and (c) 3# (230 MPa).

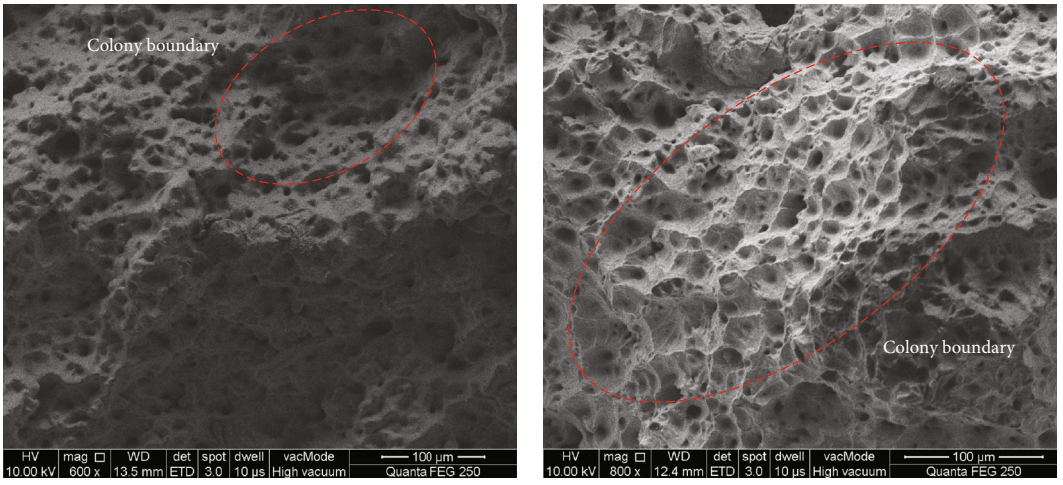

(a) (b)

Figure 4: Microstructure of fracture surface with different stresses: (a) 1# (200 MPa) and (b) 3# (230 MPa).

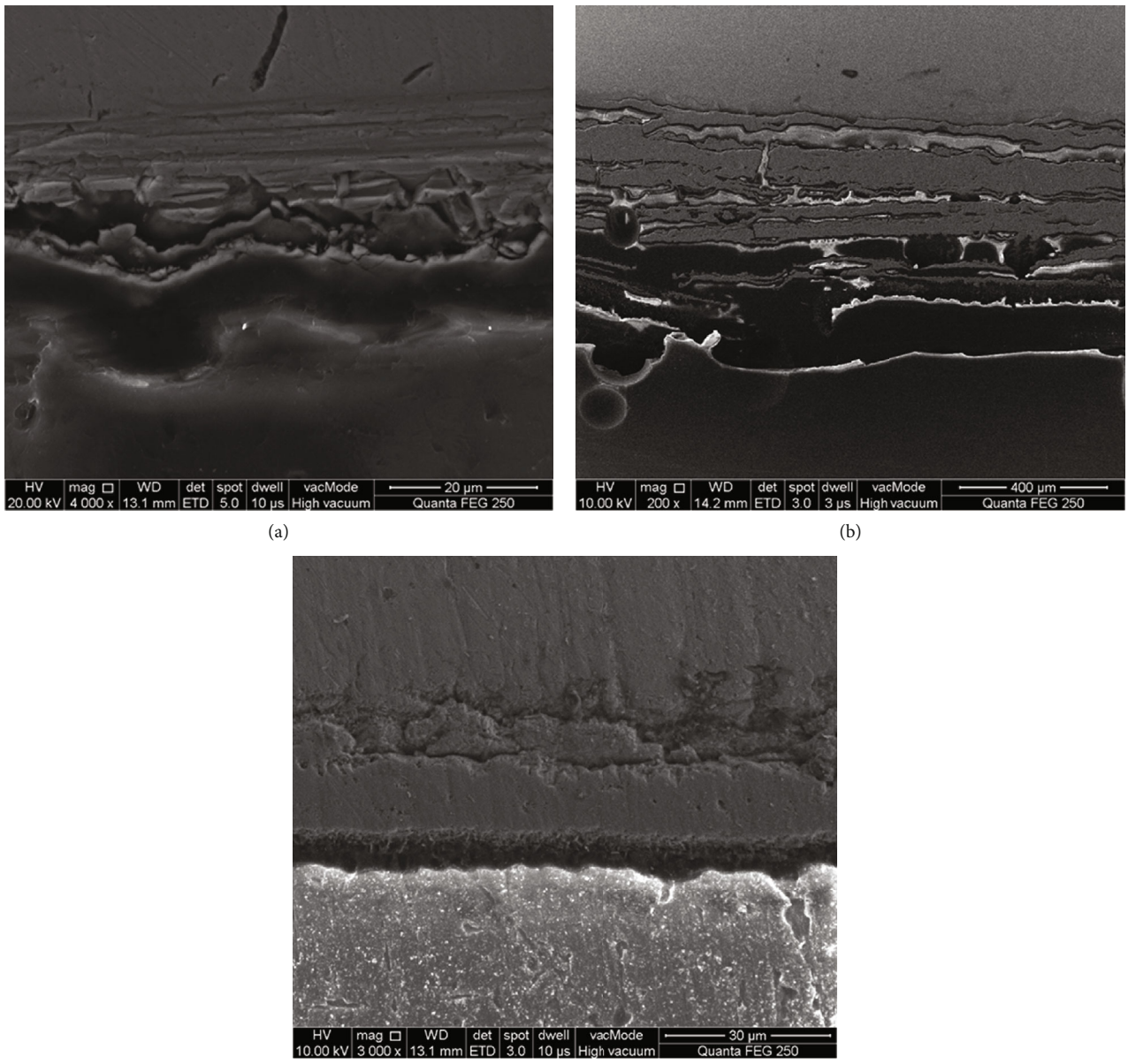

Figure 5: Morphology of corrosion layer at different temperatures: (a) 4# (560°C, mixed salt), (b) 6# (600°C, mixed salt), and (c) 7# (600°C, air).

Table 4: EDS analysis of corrosion layer.

Element	Corrosion outer layer (wt.%)	Corroded inner layer (wt.%)
Fe	78.24	75.94
O	17.17	15.06
Cr	0.48	2.78
C	3.64	4.10
Cl	0.31	1.05
Si	0.16	0.77

to a cycle. The reaction mechanism is mainly expressed by chemical equations (3)–(7) (M = Na, K),

$$2MCl + Fe_2O_3 + 1/2O_2 \longleftrightarrow M_2Fe_2O_4 + Cl_2 \quad (3)$$

$$4NaCl + Cr_2O_3 + 5/2O_2 \longleftrightarrow 2NaCrO_4 + 2Cl_2 \quad (4)$$

$$Fe + Cl_2 \longleftrightarrow FeCl_2 \quad (5)$$

$$2FeCl_2 + 3/2O_2 \longleftrightarrow Fe_2O_3 + 2Cl_2 \quad (6)$$

$$3FeCl_2 + 2O_2 \longleftrightarrow Fe_3O_4 + 3Cl_2 \quad (7)$$

At the beginning of the corrosion reaction, chlorine (Cl_2) is produced by the interaction between the chlorine salt and the metal oxides at high temperature. $FeCl_2$ is formed by

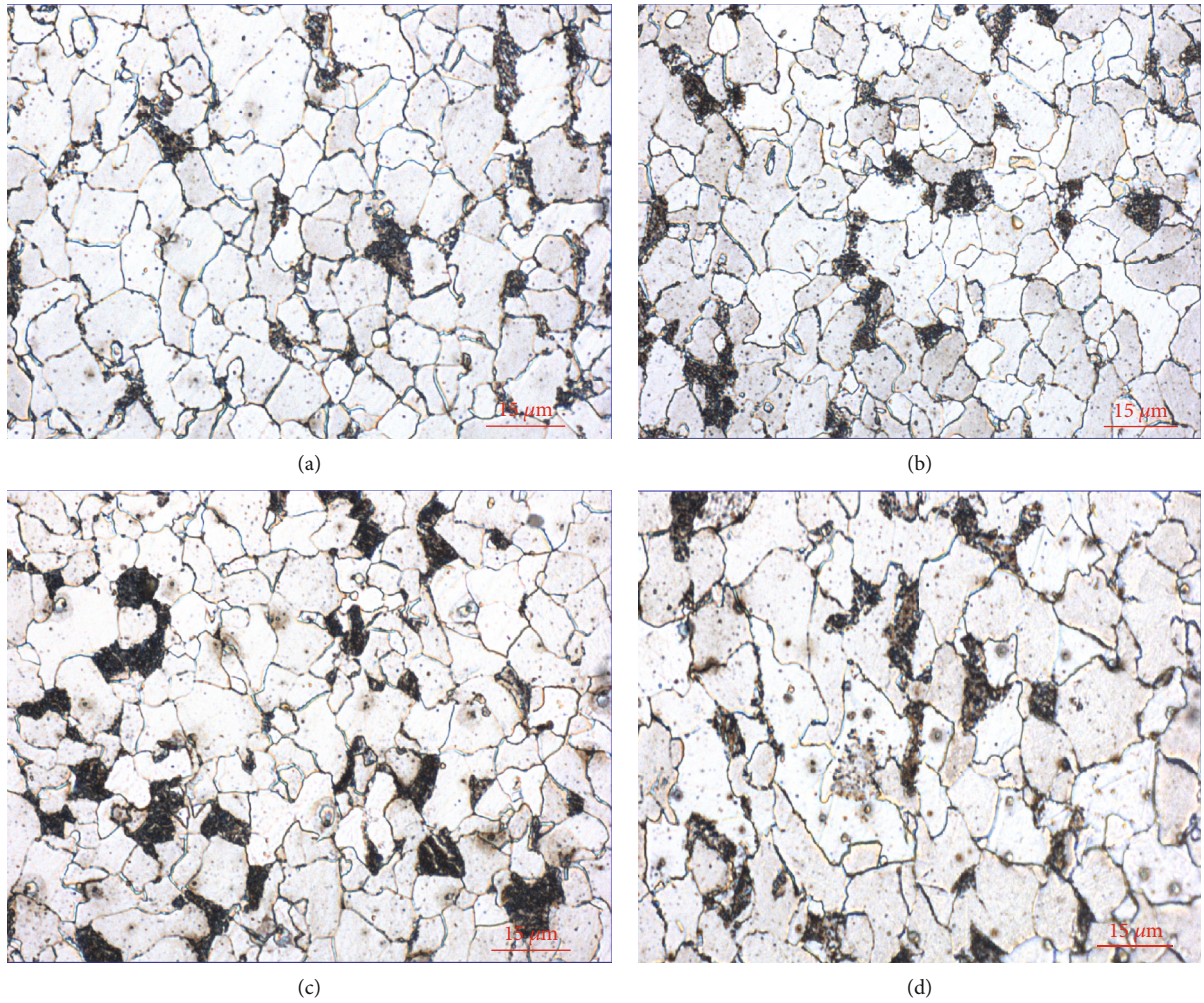

Figure 6: Metallographic diagrams in the matrix under different temperature environments: (a) 4# (560°C, mixed salt), (b) 5# (580°C, mixed salt), (c) 6# (600°C, mixed salt), and (d) 7# (600°C, air).

the formation of Cl_2, which enters into the substrate of the material through tiny holes and cracks on the surface. $FeCl_2$ is unstable and is easily transformed from solid state to gaseous state at the high-temperature environment. When the gaseous $FeCl_2$ enters the high oxygen partial pressure through the defect structure of the material, it is oxidized to Fe_2O_3 and Fe_3O_4 and releases chlorine again, which is the reason why the Cl element cannot be detected in the inner and outer layers. Due to the relatively low oxygen partial pressure between the corrosion inner and the transition layers, the EDS results show that $FeCl_2$ is not completely oxidized. Since the corrosion transition layer is close to the substrate and has relatively low oxygen content, the mass fraction of Cl in the layer is the largest. Through the above reaction equations and EDS test results, it is known that the corrosion outer layer is mainly porous Fe_2O_3 and Fe_3O_4, while the corrosion inner layer is composed of Fe_2O_3, Fe_3O_4, $FeCl_2$, and Cr_2O_3. Activated oxidation of chlorine in a high-temperature chloride salt corrosive environment is a process of gradual destruction from the surface of the material to the substrate. As long as chlorine salt is sufficient and oxygen pressure is maintained, the oxidation reaction inside the material is equivalent to a cyclic process. Therefore, the continuous activation of oxidation makes the thermal corrosion more destructive to the oxidation of specific heats.

3.4.2. Microstructure of Substrate Areas. The 12Cr1MoV matrix structure is usually composed of ferrite and pearlite, and a large amount of cementite is distributed on pearlite. With the continuous increase of temperature in the hot corrosion environment, the corresponding changes in the structure of the material matrix have also occurred. Figure 6 shows the metallographic diagrams in the matrix under different temperature environments, and Figure 7 shows SEM morphology and the corresponding EDS energy spectrum of pearlite. It can be seen from Figure 7 that the ferrite and cementite in pearlite are sandwiched with each other, with a large number and compact arrangement, and the precipitate phase appears at the grain boundary. According to Figures 6(a)–6(c), with the increase of temperature, the atomic force increases, and the long strip cementite accelerates to a point transition, partly changes into a bead shape, then accumulates into pellets and disappears from pearlite, which gradually exposes the ferrite substrate. Combined with

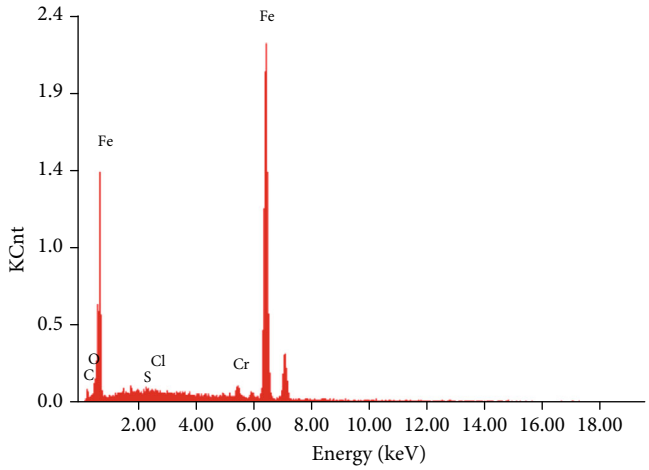

Figure 7: SEM morphology and EDS energy spectrum analysis of pearlite.

Figure 1(b), within the same experimental time, the sample at 600°C occurs fracture failure, while another samples are still in the steady-state creep stage at 560°C and 580°C. Meanwhile, the creep deformation rate of the specimen 5# (580°C) is obviously larger than that of the specimen 4# (560°C). As the strength of the material increases with the increase of pearlite number, the spheroidization can weaken the yield strength, compressive strength, and creep limit of the material and accelerate its creep deformation. On the basis of EDS analysis, the results show that the precipitates are mainly composed of 94.15% of Fe, 3.15% of C, 1.34% of Cr, and small amounts of O and Si. And by comparing the relevant research [16], the particles are $M_{23}C_6$-type carbides, in which M represents Fe and Mo elements. The results show that the number of irregular point-like precipitates gradually increases, the size becomes larger, and the surface becomes rougher. The grain boundary binding force becomes weakened, and the impact toughness and mechanical properties of the material are severely degraded. Therefore, the precipitation behavior of carbides becomes the main reason for the tensile strength of the materials under increasing temperature.

4. Conclusion

(1) Tensile creep deformation of 12Cr1MoV steel is controlled by diffusion creep at NaCl-35%KCl salt environment with 600°C

(2) Creep loading temperature has a great influence on the hot corrosion behavior of high-temperature alkali metal chloride salt. Under the same loading stress, as the temperature increases, the degree of hot corrosion deepens. Its corrosion mechanism is activated oxidation of chlorine

(3) Creep loading stress has a direct influence on the fracture failure of 12Cr1MoV steel. The nucleation grows and polymerizes to form micropores, and the micropores increase and grow in the longitudinal and lateral directions and polymerize into microcracks; the greater the stress, the faster the crack propagation, the weaker tensile performance, the shorter the steady creep phase time, and the faster the transition to the third stage of creep, resulting in rapid fracture failure

(4) The main cracks are found at the colony boundary, and the cracks primarily propagate along the colony boundary after creep testing

(5) Creep has a great influence on the matrix structure of 12Cr1MoV steel in high temperature. Increasing the temperature from 560°C to 600°C, the phenomenon of pearlite and cementite spheroidization becomes obvious and the toughness and tensile properties of the material are weakened, leading to shorter steady-state creep time and accelerating the fracture failure

Data Availability

No data were used to support this study.

Conflicts of Interest

The authors declare that they have no conflicts of interest.

Acknowledgments

This research was funded by the National Natural Science Foundation of China, grant number 51275058.

References

[1] W. Qijiang, Z. Guoli, and Z. Yedong, "Review of research developments of 12Cr1MoVG heat resistant steel in China," *Baosteel Technical Research*, vol. 11, no. 2, pp. 18–29, 2017.

[2] G. Pei, Y. Su, S. Filippeschi, and H. Zheng, "Recent research progress in solar thermal conversion theory and applications," *International Journal of Photoenergy*, vol. 2015, Article ID 850413, 2 pages, 2015.

[3] J. Yang, Q. Jiang, J. Hou, and C. Luo, "A study on thermal performance of a novel all-glass evacuated tube solar collector manifold header with an inserted tube," *International Journal of Photoenergy*, vol. 2015, Article ID 409517, 7 pages, 2015.

[4] O. Behar, A. Khellaf, and K. Mohammedi, "A review of studies on central receiver solar thermal power plants," *Renewable and Sustainable Energy Reviews*, vol. 23, no. 4, pp. 12–39, 2013.

[5] K. Vignarooban, X. Xu, A. Arvay, K. Hsu, and A. M. Kannan, "Heat transfer fluids for concentrating solar power systems - A review," *Applied Energy*, vol. 146, no. 15, pp. 383–396, 2015.

[6] S. Guillot, A. Faik, A. Rakhmatullin et al., "Corrosion effects between molten salts and thermal storage material for concentrated solar power plants," *Applied Energy*, vol. 94, no. 6, pp. 174–181, 2012.

[7] A. S. Dorcheh, R. N. Durham, and M. C. Galetz, "Corrosion behavior of stainless and low-chromium steels and IN625 in molten nitrate salts at 600 °C," *Solar Energy Materials and Solar Cells*, vol. 144, no. 6, pp. 109–116, 2016.

[8] J. J. He, W. Z. Xiong, and W. Zhang, "Investigation of high temperature corrosion behavior on superheater steels of

biomass-fired boiler in molten alkali salts mixtures," *Advances in Mechanical Engineering*, vol. 8, no. 11, pp. 1–9, 2016.

[9] W. Li, J. Chen, H. Liang, and C. Li, "Research on high-temperature compression and creep behavior of porous Cu-Ni-Cr alloy for molten carbonate fuel cell anodes," *Materials Science-Poland*, vol. 33, no. 2, pp. 356–362, 2015.

[10] K. S. Gosh, "Creep rupture of Nimonic-90 under salt-induced high temperature corrosion," *Indian Journal of Engineering & Materials Sciences*, vol. 7, no. 1, pp. 70–76, 2000.

[11] V. Suryanarayanan, K. J. L. Iyer, and V. M. Radhakrishnan, "Interaction of low temperature hot corrosion and creep," *Materials Science & Engineering A*, vol. 112, no. 6, pp. 107–116, 1989.

[12] S. Bagui, A. K. Ray, J. K. Sahu et al., "Influence of saline environment on creep rupture life of Nimonic-263 for marine turbine application," *Materials Science& Engineering A*, vol. 566, no. 20, pp. 54–60, 2013.

[13] J. He and W. Xiong, "Effect of high temperature hot corrosion on the compression creep behavior of 12Cr1MoV alloys," *High Temperature Materials and Processes*, vol. 36, no. 10, pp. 1011–1023, 2017.

[14] H. Dieringa, N. Hort, and K. U. Kainer, "Investigation of minimum creep rates and stress exponents calculated from tensile and compressive creep data of magnesium alloy AE42," *Materials Science and Engineering A*, vol. 510-511, no. 15, pp. 382–386, 2009.

[15] X. Yang, S. Li, and H. Qi, "Effect of high-temperature hot corrosion on the low cycle fatigue behavior of a directionally solidified nickel-base superalloy," *International Journal of Fatigue*, vol. 70, no. 1, pp. 106–113, 2015.

[16] Z. Li, N. Xiao, D. Li, J. Zhang, Y. Luo, and R. Zhang, "Effect of microstructure evolution on strength and impact toughness of G18CrMo2-6 heat-resistant steel during tempering," *Materials Science and Engineering: A*, vol. 604, no. 16, pp. 103–110, 2014.